State-Space Inflow Model Identification and Flight Dynamics Coupling for an Advanced Coaxial Rotorcraft Configuration

Sean Hersey **Roberto Celi**
Department of Aerospace Engineering
University of Maryland
College Park, MD

Ondrej Juhasz
San Jose State University
Ames Research Center
Moffett Field, CA

Mark B. Tischler
U. S. Army Aviation Development Directorate (AMRDEC)
Ames Research Center
Moffett Field, CA

Omri Rand **Vladimir Khromov**
Faculty of Aerospace Engineering
Technion
Haifa, Israel

ABSTRACT

In order to consider the stability and controllability of advanced coaxial configurations, a better understanding of the aerodynamic interactions between rotors is required. Modern aerodynamic analysis tools such as free wake models can accurately model the behavior of the inflow of a coaxial configuration, without the inclusion of theoretical limitations and approximations used by classical-simplified schemes. They are not, however, expressed in state-space form and therefore can not be readily analyzed as a linear flight dynamics problem and are often computationally expensive. The objective of this paper is to extend a system identification method, which was previously validated for single main rotor helicopters, to the extraction of state-space linearized models from computed inflow data acquired from free wake models of a coaxial rotor in hover. Also a key extension of the identified inflow systems is shown to model inflow off of the rotor plane as a output equation of the inflow system, or as its own ODE inflow system. With state-space models of inflow defined for an advanced coaxial configuration, this paper also presents a study of the fully coupled aircraft flight dynamics, showing key effects of rotor inflow on the dynamics of a coaxial rotorcraft configuration.

NOTATION

C_L	Aerodynamic rotor roll moment
C_M	Aerodynamic rotor pitch moment coefficient
C_T	Aerodynamic rotor thrust coefficient
$\mathbf{C}$	Array containing $\left[C_T^U \;\; C_L^U \;\; C_M^U \;\; C_T^L \;\; C_L^L \;\; C_M^L\right]^\mathsf{T}$
$\Delta\mathbf{C}$	Perturbation of $\mathbf{C}$
$\mathbf{C}_{eq}$	Equilibrium or trim value of $\mathbf{C}$
$[M]$	Induced inflow M matrix
$[L]^{-1}$	Inverse of induced inflow L matrix
$\bar{v}_x$	x-component of non-dim. off-rotor inflow
$\bar{v}_y$	y-component of non-dim. off-rotor inflow
$\bar{v}_z$	z-component of non-dim. off-rotor inflow
$\bar{\boldsymbol{v}}$	Vector containing $\left[\bar{v}_x \;\; \bar{v}_y \;\; \bar{v}_z\right]^\mathsf{T}$
λ_0	Average induced inflow coefficient
λ_{1S}	Lateral induced inflow coefficient
λ_{1C}	Longitudinal induced inflow coefficient
$\boldsymbol{\lambda}$	Array containing $\left[\lambda_0^U \;\; \lambda_{1S}^U \;\; \lambda_{1C}^U \;\; \lambda_0^L \;\; \lambda_{1S}^L \;\; \lambda_{1C}^L\right]^\mathsf{T}$
$\Delta\boldsymbol{\lambda}$	Perturbation of $\boldsymbol{\lambda}$
$\boldsymbol{\lambda}_{eq}$	Equilibrium or trim value of $\boldsymbol{\lambda}$
$[\tau]$	Time delay matrix
θ_0	Swashplate collective
θ_{1C}	Swashplate longitudinal cyclic
θ_{1S}	Swashplate lateral cyclic
$\boldsymbol{\theta}$	Array containing $\left[\theta_0^U \;\; \theta_{1S}^U \;\; \theta_{1C}^U \;\; \theta_0^L \;\; \theta_{1S}^L \;\; \theta_{1C}^L\right]^\mathsf{T}$
θ_0^S	Symmetric swashplate collective
θ_{1C}^S	Differential swashplate collective
θ_{1S}^S	Symmetric swashplate longitudinal cyclic
θ_0^D	Symmetric swashplate lateral cyclic

Superscripts

$(\ldots)^L$	Lower rotor
$(\ldots)^U$	Upper rotor

Matrix Operators

$\times$	Matrix multiplication
$\circ$	Element by element multiplication

INTRODUCTION

The next generation of military and commercial rotorcraft is expected to reach substantially higher speeds than platforms currently in production, through the use of advanced configurations. One possible configuration is a coaxial helicopter with thrust and/or lift compounding, obtained through the addition of pusher propellers and/or wings. Coaxial rotors provide clear advantages by not requiring a tail rotor and by being able to balance the dissymmetry of lift experienced by each rotor in high-speed forward flight. Unlike single main rotors,

Presented at the AHS International 73rd Annual Forum & Technology Display, Fort Worth, Texas, USA, May 9–11, 2017.
Copyright © 2017 by the Authors, All rights reserved. Approved for public release; distribution unlimited.

their maximum speed is not limited by retreating blade stall. Recent advances in design have made it feasible and worthwhile to overcome the challenges of coaxial rotors, including higher complexity, higher hub drag and higher vibratory loads.

Significant gaps remain in the fundamental understanding of the flight dynamics and control characteristics of coaxial compound rotorcraft configurations. Strong aerodynamic interactions exist between the two rotors, and between the rotors, empennage, and pusher propeller. The role of these interactions in steady flight and maneuvers has not been studied in depth and is not fully understood. Additionally, compound configurations create control redundancy and possibly novel strategies to trim and perform maneuvers.

Most building blocks of coaxial compound simulation are currently available, with the partial exception of accurate, computationally efficient models of rotor wake dynamics in the form of Ordinary Differential Equations (ODEs). Efficiency is required for real-time piloted simulation, whereas the specific ODE format is required for flight control system design and handling qualities compliance assessment. For single main rotors, this requirement is usually fulfilled by the the Peters-He finite state wake (Ref. 1) or a similar model. These momentum-theory type models have the benefit of providing a closed form solution over the entire disk.

Recently, state-space models of coaxial rotor wakes have been presented (Refs. 2–5), which can be considered as sophisticated applications of momentum theory. They are based on potential flow theory and are extensions of Peters-He dynamic inflow model to include off-rotor interference in varying ways. Ref. 2 also presents a wake in which Galerkin weighted residuals are used to discretize the momentum equation. Ref. 4 presents the potential flow solution with an active-receiving rotor model that uses Morillo-Duffy finite state formulation for off-disk inflow. These solutions, however, are not closed form and still require some manipulations for wake curvature, wake contraction and compressibility effects, which can be important for coaxial systems. Ref. 6 tries to correct for such wake distortions by using system identification on a free-wake model to identify correction factors for the potential flow solutions.

Free vortex wake-based and Computational Fluid Dynamics (CFD)-based methodologies are capable of modeling complex aerodynamic flow fields, and could represent the basis for the extraction of compact inflow models in ODE form. In Ref. 7, a dynamic inflow (Refs. 8,9) type model was extracted from free and rigid vortex wake models of a single main rotor helicopter using system identification techniques. Two different wake models and two different approaches, based on the response to single frequency excitations and to frequency sweeps, respectively, were used. A single main rotor configuration was used, and the results were subsequently incorporated in a full nonlinear flight dynamic simulation, and the results compared with flight test data. The agreement was good in the range of frequency of interest for flight dynamics. Ref. 7 was the first in the literature to show the extraction of a rotor inflow model in ODE form by system identification from a refined aerodynamic analysis.

In subsequent work by Gennaretti et al. (Refs. 10, 11), a similar methodology was applied to a boundary element method, potential flow formulation of rotor wake inflow. Frequency responses to perturbations of rotor kinematic quantities were obtained, and transfer functions were extracted using rational approximation techniques.

Many refined rotor aerodynamic theories include the ability to compute the flow field at arbitrary points in space, and not just at the rotor disk. For example, in free vortex wake methods, this is needed to compute the dynamics of the vortices that describe the rotor wake. As a consequence, it is possible to describe the flow field dynamics at other locations of practical interest, such as the empennage, and extract compact inflow models in state-space form valid at those locations.

The objectives of the paper are to present:

1. The extraction of an inflow model in ODE form for a coaxial rotor in hover using frequency domain system identification techniques.

2. The extension of the methodology of Ref. 7 to the extraction of a linear state-space model of rotor-induced inflow at locations other than the rotor disk, generally referred to as off-rotor inflow. Specifically this is applied at the horizontal tail and on the fuselage.

3. The coupling of the rotor inflow model to a full flight dynamic simulation, to show key effects of rotor inflow on the stability and frequency response of a coaxial rotorcraft configuration.

COAXIAL AIRCRAFT MODEL

A coaxial aircraft model was developed to assess the extracted inflow model. Gross sizing and rotor geometry data of the aircraft come from the "regression" military model found in Ref. 12. Blade structural and mass properties were scaled using data from the Sikorsky XH-59 Advancing Blade Concept (Ref. 13) so that the 1st lag and flap modes match those of the ABC, roughly 1.3/rev for lag and 1.5/rev for flap. The same airfoils were used as in the XH-59 (Ref. 13).

Fuselage and empennage component sizes and locations are based on Ref. 12, but the aircraft has been shortened to be more consistent with publicly available images of modern coaxial-pusher aircraft, such as the Sikorsky X2 Technology^{TM} Demonstrator (Ref. 14). General fuselage aerodynamics also come from Ref. 12. Look-up tables for horizontal and vertical stabilizer aerodynamics are based on wind-tunnel data obtained for the XV-15 (Ref. 15) and contain effects of elevator and rudder deflection, respectively. The pusher is modeled as a Bailey momentum theory type rotor (Ref. 16). However, the lack of free-stream velocity in hover means that the fuselage and stabilizers are essentially inactive, and for these results, the pusher is also assumed to also be inactive. The final configuration is shown in Fig. 1 and key sizing data is found in Table 1.

Fig. 1. Generic coaxial aircraft model (modified from original found in Ref. 12)

Table 1. Coaxial aircraft characteristics

Characteristic	English	Metric
Gross Weight	35,185 lb	15,960 kg
# Rotors	2	
Rotor Radius	30.55 ft	9.31 m
Rotor Ω	23.7 rad/s	
Rotor Spacing	14% of Radius	
# Blades per Rotor	4	
Blade Weight	1133 lb	513 kg
1ST Flap Freq.	1.5/rev	

METHODS

Aerodynamic Modeling

Two coaxial free-wake models are used, namely, the Maryland Free Wake (MFW) model (Ref. 17) and the RAPiD's (Rotorcraft Analysis for Preliminary Design) Free Wake (RFW) Model (Refs. 7, 18, 19). For the configuration used in the present study, shed wake effects are neglected, and the wake is modeled by a near wake portion that extends over a limited azimuth angle behind each blade, and a single tip vortex per blade. In both models, each vortex is discretized with linear segments defined by collocation points that are allowed to convect freely in the velocity field generated by the combination of free stream velocity and bound and trailed vorticity.

- *Maryland Free Wake (MFW)*

  The MFW is based on a time-accurate free-vortex wake method (FVM) (Ref. 20). The velocity field induced by the wake at any location is computed by application of the Biot-Savart law, and then by numerically integrating the induced velocity contribution from each vortex element over the entire flow field. The vortex filaments are approximated by straight-line segments, resulting in a prediction of the induced velocity field that is second-order accurate (Ref. 21).

  Each blade is modeled as a distribution of vortex singularities (bound vortices) in the flow field using the Weissinger-L lifting surface model (Ref. 22). The wake from each rotor blade consists of a vortex sheet and a concentrated tip vortex. In the present work, the near wake is assumed to be rigid and fixed to the blade. The near wake is truncated at 30° behind each blade, and is coupled by means of a circulation-preserving boundary condition to the far wake consisting of a single rolled-up tip vortex.

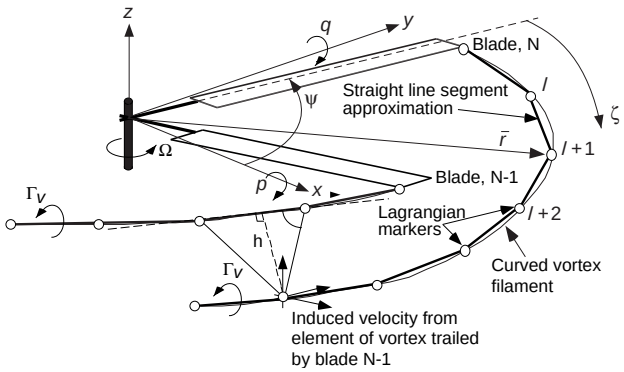

Fig. 2. Schematic showing the Lagrangian markers used to represent the rotor wake (Ref. 21).

  The vortices in the far wake are defined by the positions of Lagrangian markers that are connected by straight-line segments that approximate the otherwise curved vortex filaments; see Fig. 2. These markers are free to convect to force-free locations under the influence of the local velocity field. Their motion is obtained by solving the governing equations using a time-accurate, two-step backward, predictor-corrector scheme (PC2B) that was developed by Bhagwat and Leishman (Ref. 17).

  The MFW results in this work were obtained using tip trailed vortex filaments discretized with straight segments of length $\Delta\psi = 10°$, with the length of each filament equal to six rotor revolutions or 2160°. Shed vorticity was neglected.

- *RAPiD Free Wake (RFW)*

  The RFW models the wake by a single tip vortex per blade (of each rotor), since the analysis is focused on a generic "outer inflow solution". The said tip vortex is discretized with linear segments defined by collocation points that are allowed to convect freely in the velocity field generated by the combination of the free stream velocity, the bound and trailed vorticity. The modeling includes semi-empirical models for vortex core and vortex dissipation. Vortex core is implemented via analytical rigid wake core that is smoothly blended into the far Bio-Savart induced velocity. The vortex dissipation model creates a vortex core that grows asymptotically with the wake age. Subsequently, vortex diffusion takes a major role in creating and updating the wake geometry.

  Note that for the cases discussed in the present context, due to the wide range of possible perturbation frequencies, time and blade azimuth angle are not necessarily interchangeable as two different blades may experience different loading at the same azimuthal station. At time $t = 0$, a tip control vortex point is created at the tip of each blade with intensity, say Γ', where this vortex intensity is a function of both time and azimuth angle. After

a finite small time step, Δt, the vortex points have drifted with the local velocity induced at their various locations. At that time, a new vortex point of magnitude that correspondent to the tip vortex strength at the new blade position $\psi + \Delta\psi$ and at $t = \Delta t$ is created, say Γ'', and shifted thereafter with the local velocity as well. These two points create a vortex segment with a linear variation of magnitude that varies from Γ' to Γ''. This process is continued and a vortex line that consists of large number of segments of nonuniform strength is created. The time-dependent shape of this line is created by the time-dependent location of the above control points which are moving with the local velocity.

Clearly, the local velocity that is calculated at each control point is the total velocity that has been accumulated by all segments of all blades of all rotors. In the presence of ground/fuselage in the rotor vicinity, these are modeled using source panels which are all time-dependent and the wake is developed under the influence of these elements as well.

For both the MFW and the RFW, the calculation of the induced velocity $\mathbf{V}$ due to bound and trailed vorticity at any point of the flow field is based on the repeated application of Biot-Savart law (Ref. 23):

$$\mathbf{V} = \frac{\Gamma}{4\pi}\int_{\ell}\frac{d\ell \times \mathbf{r}}{|\mathbf{r}|^3} \tag{1}$$

where Γ is the circulation and $\mathbf{r}$ is the distance of the point from the vortex line element ℓ.

It should be noted that an accurate calculation of the induced velocity at the empennage is difficult, due to the complexity of the flow field, which includes the interaction of the rotor wake vortices with the fuselage, the effects of the empennage own bound and trailed vorticity, and the role of other configuration dependent elements, such as jet exhaust, tail rotors, and pusher propellers (Ref. 23). The models used in this study capture only some of the relevant physics, and do so in an approximate way. On the other hand, these models are adequate for the development and the illustration of the methodologies to extract state-space inflow models, because they are sophisticated and have mathematical characteristics representative of more advanced aerodynamic theories.

Coaxial Inflow Model Extraction – MFW

The model extraction methodology is essentially the same as the frequency domain system identification methodology presented in Ref. 7. For the coaxial rotor induced inflow, the model is written as a linearized extension of the Pitt-Peters model, i.e.,

$$[M]\Delta\dot{\boldsymbol{\lambda}} + [L]^{-1}\Delta\boldsymbol{\lambda} = \Delta\mathbf{C}(t - [\tau]) \tag{2}$$

where $[M]$ and $[L]^{-1}$ are the 6 by 6 constant (for a given flight condition) matrices that define the inflow model, and are extracted using frequency domain system identification methods, and $[\tau]$ is a matrix of time delays that approximates the higher order dynamics not explicitly included in the model. The Δ prefixes on the states and inputs are dropped throughout this paper for brevity, except when explicitly necessary, however all models in this paper should be assumed to be perturbation models.

Frequency Response Generation – MFW

In the present study, the following methodology is used with the MFW. First, the wake is marched forward in time until moment trim has been achieved, the wake geometry has converged to a periodic solution, and the desired input values of total thrust coefficient, as well as torque balance, have been reached. Next, frequency sweep "chirp" inputs, shown in Ref. 7, of all controls in $\boldsymbol{\theta}$ are applied, one control at a time, and the corresponding time histories of the perturbation inflow state vector $\Delta\boldsymbol{\lambda}$ and the perturbation aerodynamic load vector $\Delta\mathbf{C}$ are calculated. Therefore, $\Delta\boldsymbol{\lambda}$ and $\Delta\mathbf{C}$ are both outputs of the wake model, corresponding to the input $\boldsymbol{\theta}$.

The vectors $\Delta\mathbf{C}$ and $\Delta\boldsymbol{\lambda}$ are also, respectively, the input and outputs for the system described by Eq. (2). This is the state-space system that is extracted from the wake responses. The frequency domain system identification tool CIFER® (Ref. 24) is utilized to analyze the time histories.

In Ref. 7, it was found that using swashplate inputs θ_{1s} and θ_{1c} to excite the wake dynamics typically generated both lateral and longitudinal aerodynamic rotor loads ΔC_L and ΔC_M. These moments are the input into the linear model in Eq. (2) and must be uncorrelated (decoupled) in order for a satisfactory and unique solution to be obtained. In other words, a proper blend of all swashplate control inputs had to be determined, such that the output time histories contained only one component of the rotor aerodynamic loads, with the other as small as possible, and ideally zero. If this is not done, it is impossible to determine which portion of the output is caused by each input, e.g., which portion of λ_{1c} is caused by C_L and which by C_M (both C_L and C_M are generated by a single swashplate input, e.g., θ_{1c}), and the results will be unreliable. This issue of cross-control correlation was dealt with by introducing cross-feeds into the frequency sweeps of the control variables (swashplate inputs) to minimize the correlation between the rotor loads. Recall that, given a primary input, all other inputs will be equal to the primary input multiplied by the respective cross-feed, which can be constant or variable with frequency (for additional details on the theory see Ref. 24).

For this paper, the issue of correlation is solved without the cross-feeds through transfer function manipulation similar to the methodology shown in Ref. 11. The first step is to obtain a series of Single-Input Multiple-Output (SIMO) frequency responses of inflow and aerodynamic loads to swashplate inputs. The swashplate controls are kept decoupled by activating one at a time with a chirp input, while the other controls are held at their trim value. Each of these 6 swashplate control chirps (3 for the upper rotor and 3 for the lower rotor) produces 12 non-parametric frequency responses; 6 describing the response of $\boldsymbol{\lambda}$ and 6 describing the response of $\mathbf{C}$,

all to the given control. When the responses of all six controls are grouped in matrix form, two 6 by 6 transfer function matrices are generated. The matrix $\left[\frac{\boldsymbol{\lambda}(s)}{\boldsymbol{\theta}(s)}\right]$ describes the inflow response to swashplate inputs. The element in the i-th row and j-th column is the response of the i-th component of the inflow vector $\boldsymbol{\lambda}$ to a chirp input of the j-th component of the swashplate control vector $\boldsymbol{\theta}$ with all other controls held at their respective trim values (the notation that implies the division between two vectors is not mathematically rigorous, and is used only for clarity). The matrix $\left[\frac{\mathbf{C}(s)}{\boldsymbol{\theta}(s)}\right]$ describes the rotor aerodynamic loads response to swashplate inputs. Note that each element of the two response matrices is generally a function of frequency, therefore in practice the two matrices are three-dimensional, with frequency as the third dimension.

The desired frequency responses on inflow to aerodynamic loads can be found by numerical inversion and multiplication at each individual frequency:

$$\left[\frac{\boldsymbol{\lambda}(s)}{\mathbf{C}(s)}\right] = \left[\frac{\boldsymbol{\lambda}(s)}{\boldsymbol{\theta}(s)}\right] \times \left[\frac{\mathbf{C}(s)}{\boldsymbol{\theta}(s)}\right]^{-1} \tag{3}$$

For each frequency response in the $[\boldsymbol{\lambda}(s)/\boldsymbol{\theta}(s)]$ and $[\mathbf{C}(s)/\boldsymbol{\theta}(s)]$ matrices, and at each value of frequency, CIFER® also calculates values of the coherence. The coherence is a direct measure of the linearity between the input and output. Responses with high coherence are linear, have a high signal-to-noise ratio, and are not excited by secondary inputs (Ref. 24). It is important to assess the coherence of the $[\boldsymbol{\lambda}(s)/\mathbf{C}(s)]$ to evaluate the quality of the identification, but there is not a straightforward way to calculate the exact coherence of frequency responses obtained from the arithmetics of Eq. (3). However, from an analysis of the coherence of the individual frequency responses that go into the calculation of $\boldsymbol{\lambda}(s)/\mathbf{C}(s)$, it is possible to calculate a weighted average coherence is calculated, based on the following considerations.

1. The coherence from input to output is equal to the coherence from output to input. The coherence matrix of the inverse of a frequency response matrix must remain the same as that of the original matrix. For this method, this establishes:

$$Coh\left(\left[\frac{\mathbf{C}(s)}{\boldsymbol{\theta}(s)}\right]^{-1}_{i,j}\right) = Coh\left(\left[\frac{\mathbf{C}(s)}{\boldsymbol{\theta}(s)}\right]_{i,j}\right)$$

2. When two Single-Input Single-Output (SISO) frequency responses are multiplied, the total coherence is roughly equal to the smaller coherence of the two components. So this is used to approximate:

$$Coh\left(\left[\frac{\boldsymbol{\lambda}(s)}{\boldsymbol{\theta}(s)}\right]_{i,j} \times \left[\frac{\mathbf{C}(s)}{[\boldsymbol{\theta}(s)}\right]^{-1}_{j,i}\right) \approx \min\left\{Coh\left(\left[\frac{\boldsymbol{\lambda}(s)}{\boldsymbol{\theta}(s)}\right]_{i,j}\right), Coh\left(\left[\frac{\mathbf{C}(s)}{\boldsymbol{\theta}(s)}\right]^{-1}_{j,i}\right)\right\}$$

3. The level of coherence is unimportant if the product of two frequency responses produces a very small magnitude output, relative to the other contributing parts. Conversely, if the product of two frequency responses produces a relatively large magnitude output, then its contribution to the overall coherence is higher. This suggests that a magnitude weight based summation would be appropriate.

A singular index of the $[\boldsymbol{\lambda}(s)/\mathbf{C}(s)]$ matrix is calculated by:

$$\left[\frac{\boldsymbol{\lambda}(s)}{\mathbf{C}(s)}\right]_{i,j} = \sum_{k=1}^{6} \left[\frac{\boldsymbol{\lambda}(s)}{\boldsymbol{\theta}(s)}\right]_{i,k} \times \left[\frac{\mathbf{C}(s)}{\boldsymbol{\theta}(s)}\right]^{-1}_{k,j} \tag{4}$$

This broken down equation more clearly shows that, in this case, 6 transfer function multiplications are summed to give a value for a given index in the $\boldsymbol{\lambda}(s)/\mathbf{C}(s)$ matrix. Magnitude based weights are defined as:

$$W_{i,j}(n) = \frac{\left|\left[\frac{\boldsymbol{\lambda}(s)}{\boldsymbol{\theta}(s)}\right]_{i,n} \times \left[\frac{\mathbf{C}(s)}{\boldsymbol{\theta}(s)}\right]^{-1}_{n,i}\right|}{\left|\left[\frac{\boldsymbol{\lambda}(s)}{\mathbf{C}(s)}\right]_{i,j}\right|} \tag{5}$$

The coherence is then approximately equal to the average weighted coherence:

$$Coh\left(\left[\frac{\boldsymbol{\lambda}(s)}{\mathbf{C}(s)}\right]_{i,j}\right) \approx \sum_{n=1}^{6} \left(W_{i,j}(n) \times \min\left\{Coh\left(\left[\frac{\boldsymbol{\lambda}(s)}{\boldsymbol{\theta}(s)}\right]_{i,n}\right), Coh\left(\left[\frac{\mathbf{C}(s)}{\boldsymbol{\theta}(s)}\right]_{n,i}\right)\right\}\right) \tag{6}$$

State-Space Model Identification – MFW

The new frequency responses, combined with the approximate coherences, define the non-parametric frequency responses used to determine the state-space coaxial inflow model. These responses are analyzed using the state-space identification utility, DERIVID, within CIFER, as in Refs. 7, 24. The form of the identified state-space model is given in Eq. (2). The $[M]$, $[L]^{-1}$ and τ matrices are identified that best fit the frequency responses generated by Eq. (3).

In general, all of the responses $[\boldsymbol{\lambda}(s)/\mathbf{C}(s)]$ obtained from the free wake are nonzero and the $[M]$, $[L]^{-1}$, and τ are fully populated. This would leave a total of 108 parameters that need to be identified for the full state-space model of the coaxial system. Physical insight along with examination of the frequency responses obtained in Eq. (3) is used to reduce the number of free parameters and make the identification problem more tractable:

1. The 3-by-3 $[M]$ and $[L]^{-1}$ matrices in the Pitt-Peters dynamic inflow model are diagonal in hover, and this form is retained for the four 3-by-3 submatrices of the coaxial rotorcraft model (upper and lower rotor, and mutual interference).

2. In hover, the rotor behavior in pitch is identical to that in roll but shifted by 90°. This allows to constrain selected values of the state space matrices to be identical.

3. If a frequency response has low coherence and small magnitude, it is excluded from the identification, on the assumption that it is mostly an artifact of small nonlinearities in the system.

4. If response magnitudes are not small, but the coherences are low, the frequency responses are not considered reliable and may have to be ignored even if potentially significant. No such situation occurred in the results of this paper.

5. If the coherence is high but the magnitude is low, it may be safe to assume that it is negligible and set the corresponding transfer function to zero.

6. The form of $[M]$, $[L]^{-1}$, and τ is assumed to correspond directly to the form of $[\boldsymbol{\lambda}(s)/\mathbf{C}(s)]$, in the sense that if the magnitude of the $\{i,j\}$ component of $\boldsymbol{\lambda}(s)/\mathbf{C}(s)$ is below some preassigned threshold at all frequencies, then the $\{i,j\}$ component of the state space matrices can be set to zero.

Combining all these criteria, in hover the preliminary form of $[M]$ and $[L]^{-1}$ was found to be (only nonzero terms are shown):

$$[M] = \begin{bmatrix} m_{11} & & & m_{14} & & \\ & m_{22} & & & m_{25} & \\ & & m_{33} & & & m_{36} \\ m_{41} & & & m_{44} & & \\ & m_{52} & & & m_{55} & \\ & & m_{63} & & & m_{66} \end{bmatrix}$$

$$[L]^{-1} = \begin{bmatrix} l_{11} & & & l_{14} & & \\ & l_{22} & & & l_{25} & \\ & & l_{33} & & & l_{36} \\ l_{41} & & & l_{44} & & \\ & l_{52} & & & l_{55} & \\ & & l_{63} & & & l_{66} \end{bmatrix} \tag{7}$$

$$[\tau] = \begin{bmatrix} \tau_{11} & & & \tau_{14} & & \\ & \tau_{22} & & & \tau_{25} & \\ & & \tau_{33} & & & \tau_{36} \\ \tau_{41} & & & \tau_{44} & & \\ & \tau_{52} & & & \tau_{55} & \\ & & \tau_{63} & & & \tau_{66} \end{bmatrix}$$

with the following parameters constrained to be identical:

$$\begin{array}{cccc} m_{22}=m_{33} & m_{44}=m_{55} & m_{25}=m_{36} & m_{52}=m_{63} \\ l_{22}=l_{33} & l_{44}=l_{55} & l_{25}=l_{36} & l_{52}=l_{63} \\ \tau_{22}=\tau_{33} & \tau_{44}=\tau_{55} & \tau_{25}=\tau_{36} & \tau_{52}=\tau_{63} \end{array}$$

Time Domain Verification – MFW The identified state-space model can then be validated using another CIFER utility, VERIFY, which performs time-domain verification. A new set of controls, different from the frequency sweeps used in the identification, is applied to the the MFW to get new time histories of $\Delta\boldsymbol{\lambda}$ and $\Delta\mathbf{C}$. VERIFY then uses the time histories of $\Delta\mathbf{C}$ as inputs to a linear simulation based on the state-space system previously identified, calculating the corresponding outputs $\Delta\boldsymbol{\lambda}$. These can be directly compared with the MFW time histories to ensure adequate agreement (Ref. 24).

Off-Rotor Induced Velocity Identification

Free vortex wake models must be able to calculate the induced velocity at arbitrary locations of the flow field, because that velocity is needed to define the motion of the blade vortices. This can also be used to compute the velocity induced by the rotor wake at any other points of interest, e.g., on the horizontal tail or across the fuselage. Two methods were explored for identifying the induced velocity off of the rotor plane.

Off-rotor ODE model Inflow – RFW For each point of interest in the flowfield, a "dynamic inflow like," ODE-based model can be obtained using the same methodology as for the rotor. This approach was performed on several points across the 1/4 chord line of the horizontal tail. The *Single Frequency Analysis* for on-rotor inflow was designed to directly extract all elements of the $[M]$ and $[L]^{-1}$ matrices for a given single frequency excitation of the RFW, see Rand et al. (Ref. 7) and Rand and Khromov (Ref. 25).

To calculate the induced velocity at an off-rotor point, a similar approach has been adopted, presented here using the RFW. For a single rotor, the equation is written:

$$[M]\begin{pmatrix} \dot{\bar{v}}_x \\ \dot{\bar{v}}_y \\ \dot{\bar{v}}_y \end{pmatrix} + [L]^{-1}\begin{pmatrix} \bar{v}_x \\ \bar{v}_y \\ \bar{v}_z \end{pmatrix} = \begin{pmatrix} \Delta C_T \\ \Delta C_L \\ \Delta C_M \end{pmatrix}. \tag{8}$$

where $\bar{v}_x$, $\bar{v}_y$, $\bar{v}_z$ are the induced velocity components in the x,y,z directions, respectively.

For a coaxial rotor system, the upper rotor contributions to $\bar{v}_x$, $\bar{v}_y$, $\bar{v}_z$ are distinguished from the lower rotor contributions to the same components:

$$[M_U]\begin{pmatrix} \dot{\bar{v}}_x \\ \dot{\bar{v}}_y \\ \dot{\bar{v}}_z \end{pmatrix}_U + [L_U]^{-1}\begin{pmatrix} \bar{v}_x \\ \bar{v}_y \\ \bar{v}_z \end{pmatrix}_U = \begin{pmatrix} \Delta C_T \\ \Delta C_L \\ \Delta C_M \end{pmatrix}_U \tag{9}$$

and

$$[M_L]\begin{pmatrix} \dot{\bar{v}}_x \\ \dot{\bar{v}}_y \\ \dot{\bar{v}}_z \end{pmatrix}_L + [L_L]^{-1}\begin{pmatrix} \bar{v}_x \\ \bar{v}_y \\ \bar{v}_z \end{pmatrix}_L = \begin{pmatrix} \Delta C_T \\ \Delta C_L \\ \Delta C_M \end{pmatrix}_L \tag{10}$$

Figure 3 summarizes the methodology.

As will be shown, following a trim solution with RFW, the induced velocity at a given location due to the upper

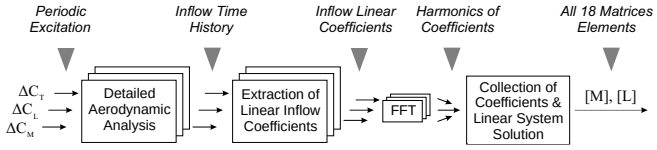

Fig. 3. Single Frequency Analysis

rotor $\vec{v}_i^U(\psi_1) = \vec{v}_x^U\hat{x} + \vec{v}_y^U\hat{y} + \vec{v}_z^U\hat{z}$ is determined for various $\Delta C_T^U(\psi_1)$, $\Delta C_L^U(\psi_1)$, $\Delta C_M^U(\psi_1)$ periodic perturbations. Similarly, the induced velocity at the same location due to the lower rotor $\vec{v}_i^L(\psi_1) = \vec{v}_x^L\hat{x} + \vec{v}_y^L\hat{y} + \vec{v}_z^L\hat{z}$ is determined for various $\Delta C_T^L(\psi_1)$, $\Delta C_L^L(\psi_1)$, $\Delta C_M^L(\psi_1)$ periodic perturbations.

These are FFT analyzed. For the upper rotor influence, the sine and cosine components (at the perturbation frequency) $\Delta\vec{v}_x^{Us}, \Delta\vec{v}_x^{Uc}$, $\Delta\vec{v}_y^{Us}, \Delta\vec{v}_y^{Uc}$, $\Delta\vec{v}_z^{Us}, \Delta\vec{v}_z^{Uc}$, are first obtained. These coefficients are then used to determine all 18 coefficients that appear in the $[M_U]$ and $[L_U]$ matrices - see Rand and Khromov (Ref. 25). Similar procedure is executed for the lower rotor influence.

Off-Rotor Output Equation

Depending on the location of interest, a simpler approach is possible that expresses the inflow at that location as an output equation, i.e., as a linear combination of rotor inflow states, with the possible addition of a time delay, and no additional states. This approximation can be sufficiently accurate because the spatial details of the flow field tend to be unimportant for the flight dynamic behavior. Furthermore, the inflow model can be extracted using only the low frequency portion, between 1 to 5 rad/s, of the frequency response, because for flight dynamics purposes, this is the region of interest.

In the present study, the methodology is applied to the extraction of a model for the average inflow along the 1/4 chord line of the horizontal tail. Although only the component of the main rotor inflow normal to the rotor disk is used in the identification, all three components of the inflow at the tail are considered. Therefore, the three inflow components are defined by the following model:

$$\begin{Bmatrix} \bar{v}_x \\ \bar{v}_y \\ \bar{v}_z \end{Bmatrix} = \begin{bmatrix} K_{0x} & K_{1cx} & K_{1sx} \\ K_{0y} & K_{1cy} & K_{1sy} \\ K_{0z} & K_{1cz} & K_{1sz} \end{bmatrix} \times \begin{Bmatrix} \lambda_0(t-\tau_0) \\ \lambda_{1c}(t-\tau_{1C}) \\ \lambda_{1s}(t-\tau_{1S}) \end{Bmatrix} \quad (11)$$

where, for example, the notation $\lambda_0(t-\tau_0)$ denotes the value of λ_0 delayed by τ seconds. The 9 constants K and the 3 delays τ in Eq. (11) are the unknowns of the identification problem.

The methodology was also applied to points on the fuselage. In this case, a similar spread of points as for the horizontal tail were calculated in order to still get an average, but they were located below the rotor. The form used for fuselage inflow was different, using up to nine time delays:

$$\begin{Bmatrix} \bar{v}_x \\ \bar{v}_y \\ \bar{v}_z \end{Bmatrix} = \begin{bmatrix} K_{0x} & K_{1cx} & K_{1sx} \\ K_{0y} & K_{1cy} & K_{1sy} \\ K_{0z} & K_{1cz} & K_{1sz} \end{bmatrix} \circ \begin{bmatrix} t-\tau_{0x} & t-\tau_{1cx} & t-\tau_{1sx} \\ t-\tau_{0y} & t-\tau_{1cy} & t-\tau_{1sy} \\ t-\tau_{0z} & t-\tau_{1cz} & t-\tau_{1sz} \end{bmatrix} \times \begin{Bmatrix} \lambda_0 \\ \lambda_{1c} \\ \lambda_{1s} \end{Bmatrix} \quad (12)$$

where $\bar{v}_x, \bar{v}_y$, and $\bar{v}_z$ are the average induced velocity components at the 1/4 chord of the horizontal tail, non-dimensionalized by tip-speed, and the λ's are the inflow harmonics at the rotor disks. The problem unknowns are the gains K and the time delays τ. As an illustration of the notation of Eq. (12), consider the expansion of the $\bar{v}_x$ inflow component:

$$\bar{v}_x = K_{0x}\lambda_0(t-\tau_{0x}) + K_{1cx}\lambda_{1c}(t-\tau_{1cx}) + K_{1sx}\lambda_{1s}(t-\tau_{1sx})$$

Equation (11) is written for a single main rotor, and for this paper, results are only shown for the single main rotor case (same configuration as Ref. 7), but the extension to coaxial rotors is straightforward. The frequency domain identification procedure for the off-rotor inflow equation is very similar to the method for the rotor inflow, and in fact it can be carried out at the same time. The non-parametric frequency response that is calculated is now $\begin{bmatrix} \bar{\boldsymbol{v}}(s) \\ \overline{\boldsymbol{\lambda}}(s) \end{bmatrix}$ and, similarly to Eq. (3), is calculated by:

$$\begin{bmatrix} \bar{\boldsymbol{v}}(s) \\ \overline{\boldsymbol{\lambda}}(s) \end{bmatrix} = \begin{bmatrix} \bar{\boldsymbol{v}}(s) \\ \overline{\boldsymbol{\theta}}(s) \end{bmatrix} \times \begin{bmatrix} \boldsymbol{\lambda}(s) \\ \overline{\boldsymbol{\theta}}(s) \end{bmatrix}^{-1} \quad (13)$$

The procedure is generally the same. To get the form given by Eq. (11) or (12), each transfer function must be fit with a constant plus time delay. Following this, time-domain verification can be performed on these equations in the same way as for the rotor inflow equations, except that the input will now be $\boldsymbol{\lambda}$ and the output will be $\bar{\boldsymbol{v}}$.

Full Aircraft Coupled Model

To analyze the effect of inflow dynamics on the full aircraft response, the state-space rotor inflow models extracted as described in the previous sections were incorporated into the full nonlinear flight dynamics simulation HeliUM. The mathematical model in HeliUM has been described in detail in Ref. 26, and only its main features will be summarized here.

The analysis is based on a "quasi-multibody" formulation, with fully numerical kinematics, flexible bodies arranged with an open-chain, tree-like topology, floating and co-rotational reference frames, but no algebraic equations of constraints. The rotors flap-lag-torsion dynamics are modeled using nonlinear finite elements (Ref. 27). Blade aerodynamics are quasi-steady, with look-up tables for lift, drag and pitching moment coefficients as a function of Mach number and incidence angle, and radial flow drag corrections (Ref. 28).

Three types of solution of the equations of motion are available, namely: (i) trim, (ii) time marching response, and (iii) linearized analysis. The calculation of a steady state equilibrium condition, or trim, is formulated as a system of nonlinear algebraic equations, and does not require that the mathematical model be in ODE form. In particular free wake or CFD-type calculation of rotor inflow can be used directly. All trim calculations for the fully coupled aircraft results were performed using the free wake in its original, finite difference-based formulation. The time marching response to pilot inputs is formulated as the solution of a system of ODEs, but portions of the models not in ODE form can be used (see Ref. 26 for details concerning the coupling of these portions). The third type of solution, i.e., linearized analysis, requires the extraction of a linearized model in state space form. To accomplish this, the entire simulation model must be in state-space form.

The linearized results of the present paper were obtained using two types of state-space rotor inflow models. The first type, used for most results, is the model extracted from the MFW using the methodology described in the previous section. The second type, used for comparison for a few coaxial results, is a simple extension of the single rotor Peters-He model (similar to Ref. 14), obtained by putting the lower rotor into a climb equivalent to the upper rotor's MFW trim average induced inflow.

Lastly, perturbation inflow states can be calculated using the MFW identified state-space model, assuming that values for equilibrium, $\mathbf{C}_{eq}$ and $\boldsymbol{\lambda}_{eq}$, are known. These can be calculated from the standalone MFW or by HeliUM trimmed with the loosely coupled MFW. Now with Eq. (2), perturbation inflow states can be calculated, given that $\Delta\mathbf{C}$ is first calculated by:

$$\Delta\mathbf{C} = \mathbf{C} - \mathbf{C}_{eq} \tag{14}$$

With perturbation inflow states, inflow at a point on the rotor disk is calculated as:

$$\boldsymbol{\lambda} = \Delta\boldsymbol{\lambda} + \boldsymbol{\lambda}_{eq} \tag{15}$$

$$\lambda(\frac{r}{R}, \psi, *) = \lambda_0^* + \lambda_{1S}^* \frac{r}{R} sin(\psi) + \lambda_{1C}^* \frac{r}{R} cos(\psi)$$

where $*$ superscripts indicates lower (L) or upper (U) rotor, depending on which is being calculated

ODEs with time delays can not be directly solved by a generic ODE solver, and specifically require a Delay Differential Equation (DDE) solver. To avoid this complication, Padé approximations are used to approximate the time delays (Ref. 29). Each time delay is written as:

$$T_{i,j}(s) = e^{-\tau_{i,j}s} = \frac{e^{-\tau_{i,j}s/2}}{e^{\tau_{i,j}s/2}} \approx \frac{1 - \tau s/2 + \tau^2 s^2/12 \ldots}{1 + \tau s/2 + \tau^2 s^2/12 \ldots} \tag{16}$$

The Padé approximant is truncated to the first order term or the second order term, depending on the length of the time delay. Larger time delays require the second order term to ensure that the error in the approximation is small. The full time delay transfer function matrix, $T(s)$, can now be used to modify the state-space model written in transfer function form:

$$\left[\frac{\boldsymbol{\lambda}(s)}{\mathbf{C}(s)}\right]_{TDA} = \frac{\boldsymbol{\lambda}(s)}{\mathbf{C}(s)} \circ T(s) \tag{17}$$

(where the "TDA" subscript indicates "Time Delays Absorbed"). The new transfer function, with the time delays absorbed, can then be converted back to state-space form. The new state space form will have added states that correspond to the poles and zeros of the time delays. The current analysis required nine time delays which became 26 time delay states. The simplicity of the 26 time delay equations ensures that they are simple for the ODE solver to solve and there is no noticeable effect on computation time.

RESULTS FOR HOVER

State-Space Model Identification Results – MFW

A state-space inflow model characteristic of the coaxial configuration in hover is identified using the methodology described in the previous sections on the MFW. Figure 4 shows the perturbation responses of upper, in black, and lower, in gray, rotor average induced inflow to a thrust perturbation of the upper rotor. The solid lines show the non-parametric frequency response, and the dashed show their best parametric fit for the given state space form given by Eqn. 7.

Table 2 show the costs of all of the transfer function fits, as well as the average. Generally, costs below 200 are considered acceptable (Ref. 24). The majority of the responses are well represented by the low-order form of the model, with the collective on-axis having costs of $J < 50$, meaning an excellent fit is obtained. The lower rotor on-axis moment response have the largest costs, meaning the form used may not be adequate for capturing the dynamics in the frequency range of the fit.

There are several interesting things to note from these frequency responses. First, the response of the upper and lower rotor are just about equal in magnitude over the full frequency range.

The non-parametric response show that at the lowest frequency (1 rad/s), the upper rotor response is slightly larger than the lower rotor response. On the other hand, in the middle frequency band, there is a larger λ_0^L response than λ_0^U response, before falling back below at high frequency. It is important to note that these responses have very high coherences, as shown by the bottom plot in Figure 4. The coherence is very close to one across the whole frequency range. Therefore, the dynamics of the wake in this frequency range are in fact very linear time-invariant. A larger set of equations describing the inflow dynamics could be produced which would perfectly fit the magnitude and phase curves, and such a system would inevitably capture more of the wake behavior. However for this paper, the state space model is constrained to the first order form given by Eq. (7), and so some error is expected.

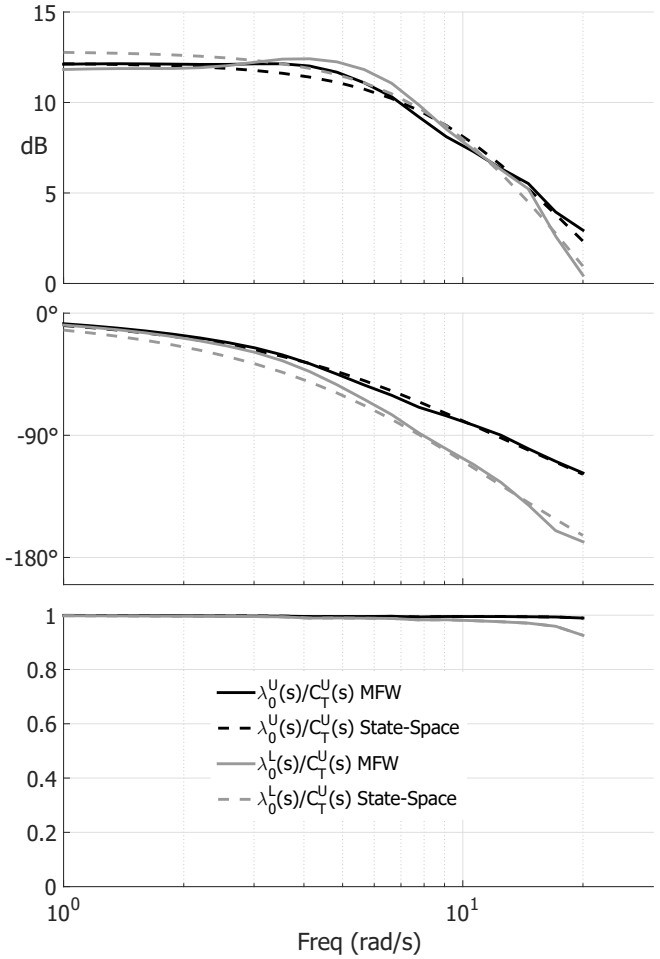

Fig. 4. Responses of λ_0^U and λ_0^L to C_T^U showing MFW non-parametric model vs the state-space parametric model; magnitude(top), phase(middle), and coherence(bottom)

The C_T^U responses from Fig. 4 are close to first order and are well fit with very low error by a first order system. However, a better fit could be possible with a second order inflow response, especially in the region of the apparent rise of the λ_0^L response at mid frequency. Because only a first order approximation is used, the state-space optimization fits the system with a slightly higher gain to account for the higher magnitude in the middle frequencies.

The opposite response, C_T^L to λ_0^U and λ_0^L, is shown in Fig. 5. Relative to the effects of C_T^U perturbations, C_T^L perturbations have a much smaller effect on both inflows. In particular, the lower rotor thrust perturbations have very little effect on the upper rotor inflow. Also the upper rotor thrust perturbations have a larger effect on the lower rotor inflow than lower rotor thrust does over the entire frequency range (as was shown in Fig. 4). The non-parametric frequency responses seem to be second order in nature and are not well modeled by the first order model structure assumed in this analysis. Physical insights and modeling of higher-order forms of dynamic inflow responses are out of the scope of this paper, and so the model was set up to follow a first-order dynamic inflow type form.

Table 2. Cost of state-space parameterizations

Response	Cost
$\lambda_0^U(s)/C_T^U(s)$	3.74
$\lambda_0^L(s)/C_T^U(s)$	17.19
$\lambda_{1C}^U(s)/C_M^U(s)$	203.97
$\lambda_{1C}^L(s)/C_M^U(s)$	178.05
$\lambda_{1S}^U(s)/C_L^U(s)$	204.08
$\lambda_{1S}^L(s)/C_L^U(s)$	177.73
$\lambda_0^U(s)/C_T^L(s)$	85.34
$\lambda_0^L(s)/C_T^L(s)$	28.82
$\lambda_{1C}^U(s)/C_M^L(s)$	115.78
$\lambda_{1C}^L(s)/C_M^L(s)$	463.61
$\lambda_{1S}^U(s)/C_L^L(s)$	115.07
$\lambda_{1S}^L(s)/C_L^L(s)$	462.45
Average Cost	171.3190

Figure 6 shows the responses of the upper and lower longitudinal inflow to the upper rotor pitching moment. Once again, the upper rotor effect on the lower rotor is roughly the same magnitude as effect on the upper rotor, indicating large coupling. Both of these responses require time delays to help fit the higher order unmodeled dynamics. The lower rotor requires a significantly larger time delay, as displayed by the larger phase roll-off. Though not shown here, the equivalent responses of C_L^U to λ_{1S}^U and λ_{1S}^L are almost exactly the same, due to hover rotor symmetry. These responses again demonstrate that a first-order inflow model structure may not be adequate in capturing all the dynamics of a coupled coaxial rotor system.

In the same manner as the C_T^L responses, Fig. 7 shows a dissimilar effect on both rotors longitudinal induced inflow caused by pitching moments of the lower rotor, C_M^L. The response of λ_{1C}^L is much larger than the response of λ_{1C}^U, indicating relatively little upper rotor coupling. Also comparing the response of λ_{1C}^L of this figure with the same response on Figure 6 shows that for the lower rotor, excitations from the upper rotor have a larger magnitude than self-induced excitation from the lower rotor.

As shown in Table 2, the cost of this state-space fit is rather high at 463.61, well above the guideline of 200. In particular, the response has a large amount of error at low frequency in both phase and magnitude, meaning that when these ODE systems are used with slow maneuvers, there will be more λ_{1C}^L created per unit of C_M^L and will be off of the correct phase by about 45 degrees. The state-space model identified is as accurate as possible given the system's first order constraint.

The identified state-space parametric model for these plots is in the form of Eq 2 with:

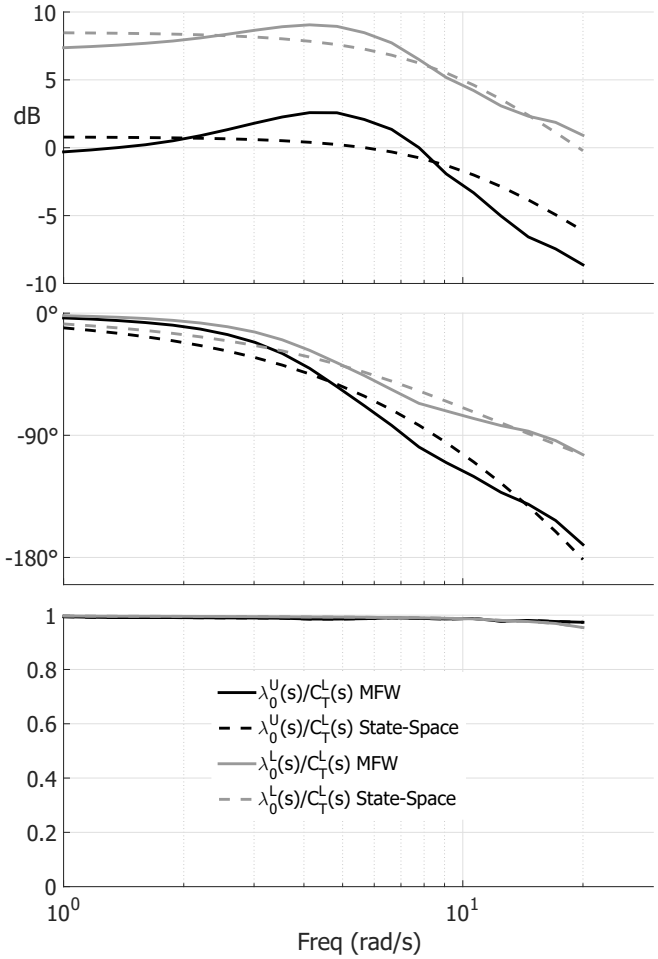

Fig. 5. Responses of λ_0^U and λ_0^L to C_T^L showing MFW non-parametric model vs the state-space parametric model; magnitude(top), phase(middle), and coherence(bottom)

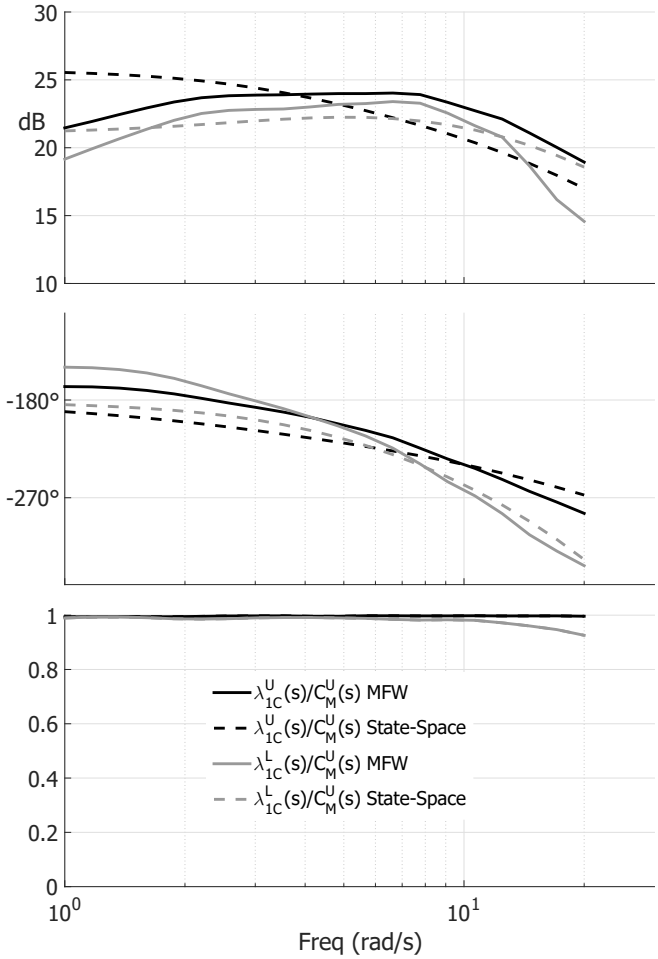

Fig. 6. Responses of λ_{1C}^U and λ_{1C}^L to C_M^U showing MFW non-parametric model vs the state-space parametric model; magnitude(top), phase(middle), and coherence(bottom)

$$[M] = \begin{bmatrix} 0.851 & 0 & 0 & -0.4664 & 0 & 0 \\ 0 & -0.243 & 0 & 0 & 0.06601 & 0 \\ 0 & 0 & -0.243 & 0 & 0 & 0.06601 \\ 0.674 & 0 & 0 & 1.0563 & 0 & 0 \\ 0 & 0.3349 & 0 & 0 & -0.27 & 0 \\ 0 & 0 & 0.3349 & 0 & 0 & -0.27 \end{bmatrix}$$

$$[L]^{-1} = \ldots$$

$$\begin{bmatrix} 0.4418 & 0 & 0 & -0.182 & 0 & 0 \\ 0 & -0.0453 & 0 & 0 & -0.01089 & 0 \\ 0 & 0 & -0.0453 & 0 & 0 & -0.01089 \\ -0.7262 & 0 & 0 & 0.6748 & 0 & 0 \\ 0 & 0.03581 & 0 & 0 & -0.06139 & 0 \\ 0 & 0 & 0.03581 & 0 & 0 & -0.06139 \end{bmatrix}$$

$$[\tau] = \begin{bmatrix} 0.03373 & 0 & 0 & 0.09985 & 0 & 0 \\ 0 & 0.02264 & 0 & 0 & 0.1265 & 0 \\ 0 & 0 & 0.02264 & 0 & 0 & 0.1265 \\ 0 & 0 & 0 & 0.02631 & 0 & 0 \\ 0 & 0.08218 & 0 & 0 & 0 & 0 \\ 0 & 0 & 0.08218 & 0 & 0 & 0 \end{bmatrix} \tag{18}$$

Time-Domain Verification Results – MFW

The inflow models were validated in the time-domain using control inputs that were smooth doublets. The first was a doublet on symmetric collective θ_0^S which produced a similar looking doublet in both C_T^U and C_T^L. Figure 8 shows these thrust responses in the top axes. The middle and bottom axes show the λ_0^L and λ_0^U responses from the identified linear model, and are compared to the actual time histories produced by MFW. In general the agreement is good. The high frequency oscillation in the λ_0^L MFW response is caused by blade-vortex interaction caused when the lower rotor blades hit the upper rotor's wake. Most of the error in the two plots can be directly attributed to the error in the state-space fits shown in figures 4 and 5.

A doublet that excited the longitudinal inflow was also performed and shown in figure 9. This doublet was performed on θ_{1C}^U creating doublets in both C_M^U and C_M^L. The corresponding time histories for λ_{1C}^U and λ_{1C}^L are shown in the middle and bottom plots, respectively. The error is slightly larger than for the collective doublet case, but the general trend is still well captured. The error is larger due to the larger differ-

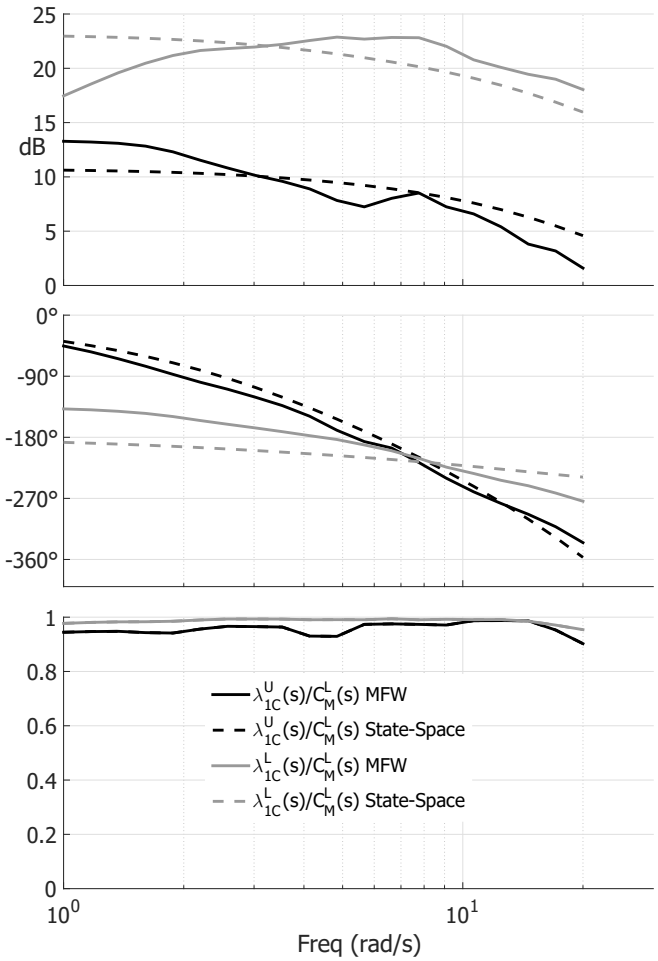

Fig. 7. Responses of λ^U_{1C} and λ^L_{1C} to C^L_M showing MFW non-parametric model vs the state-space parametric model; magnitude(top), phase(middle), and coherence(bottom)

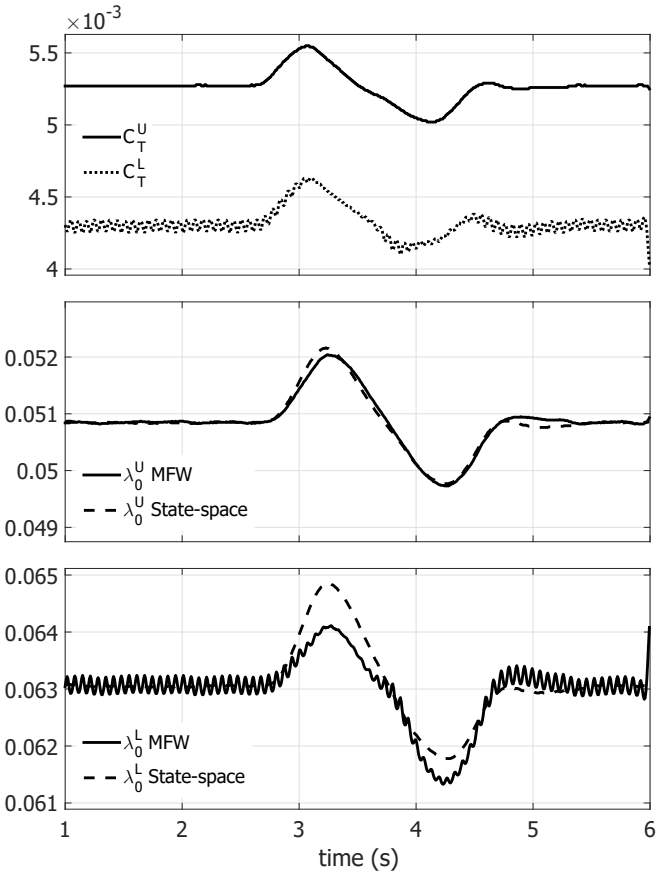

Fig. 8. Time-domain verification of symmetric collective θ^S_0 doublet, showing the thrust pertubations and the resulting time histories of λ^U_0 and λ^L_0 from the identificed state-space model and the MFW

ence between the identified state-space model and the MFW frequency response data, previously pointed out in figures 6 and 7.

Full Coupled Helicopter Results

When the identified state-space models are introduced into the full aircraft simulation, the entire mathematical model of the helicopter can be linearized to create linearized state and controls matrices. These responses can be compared to the frequency responses derived with the simplified coaxial extension of the single rotor Peters-He dynamic inflow model, obtained by simply placing the lower rotor in a climb corresponding to the average inflow of the upper rotor. Figure 10 shows the heave velocity response to the symmetric collective. Very close agreement is shown between the two responses, meaning the identified hover inflow model aligns well with the extended Peters-He model. Figure 11 shows almost perfect agreement for the yaw rate response to differential collective.

The roll and pitch response using the identified state-space model differ from the extended Peters-He model. As shown in figure 12, the MFW state-space inflow model shows the aircraft having a higher response in roll due to θ^S_{1S} than is predicted with the extended Peters-He model with the lower rotor in climb. This response elevation occurs right around the frequency range of control system crossover (1-10 rad/s), and would have a direct impact on predicted aircraft stability margins.

Figure 13 shows a similar result for the response of pitch rate to θ^S_{1C}. This response is not exactly the same as the roll rate due to the large variation in pitch and roll inertia of the aircraft. There are also small but non-zero off-axis responses, as in θ^S_{1S} causes some pitch rate and θ^S_{1C} causes some roll rate. This is indicative of the fact that the swash-plate angle is set to zero for both cases to allow comparison. Practically, the differences in the two responses may indicate that the design of the swash-plate phasing would be different depending on which inflow model is used.

Looking at the previous bode plots it is clear that the heave and directional responses are pretty much the same at high frequency, regardless of the inflow model used. The low frequency poles are different but poles above 10 rad/s are essentially unchanged. This is further shown in Tables 3 and 4 in the appendix, which show the poles of the linearized state ma-

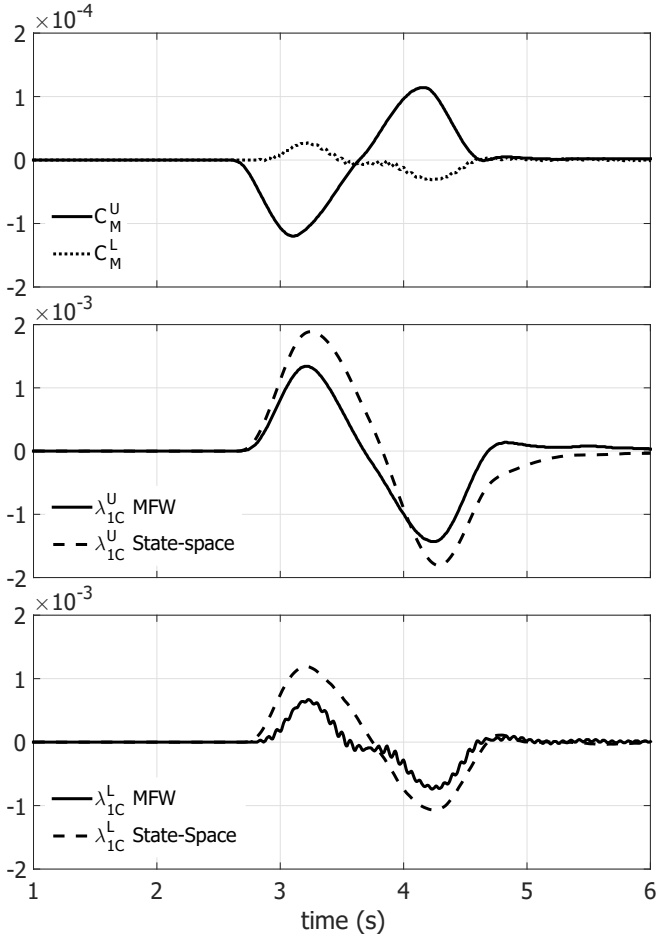

Fig. 9. Time-domain verification of upper rotor longitudinal cylcic θ_{1C}^{U} doublet, showing the pitching moment pertubations and the resulting time histories of λ_{1C}^{U} and λ_{1C}^{L} from the identificed state-space model and the MFW

trices for the two different systems. The high frequency rotor modes are very close in value when using either inflow model.

Inflow Extraction at Off-Rotor Locations

Tail ODE Induced Inflow Results – RFW The methodology prescribed for calculating an off-rotor ODE inflow model was applied to the RFW at the previously stated points of the tail. Figure 14 shows the induced velocity without excitations at three points across the 1/4 chord line of the horizontal tail at a trim C_T of 0.005. The center point lies on the longitudinal axis and the port tip and starboard tip are located at the wing tips of their respective sides. All of these points lie outside of the wake in hover. As shown, these velocities are periodic which stands in contrast with the steady nature of λ_0, λ_{1s}, λ_{1c} (without excitations) in standard dynamic inflow analysis.

Figure 15 shows the velocities at the tail center point due to thrust, roll moment and pitch moment perturbations in hover (trim $C_T = 0.005$). The small fluctuations are the rotor periods which demonstrate the fact that in this case the perturbation is relatively slow ($\tilde{\omega} = 0.2$)

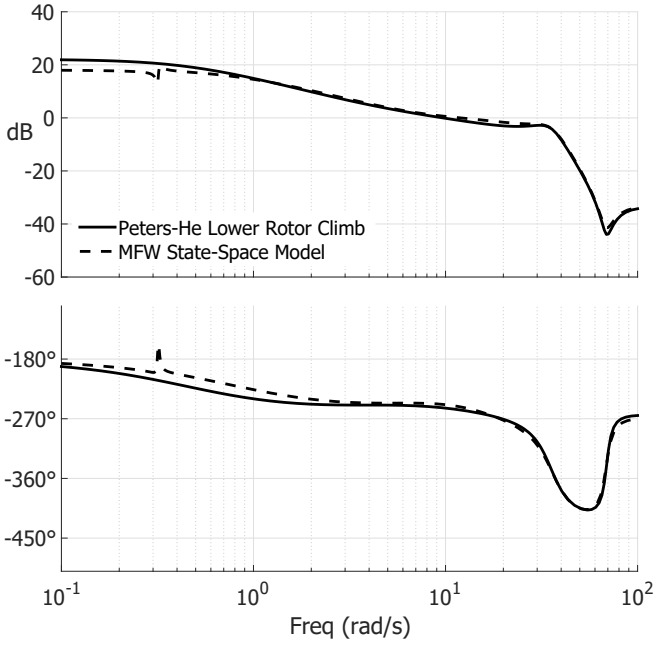

Fig. 10. Responses of heave velocity w to θ_0^S showing comparison between MFW identified state-space model and Peters-He model with the lower rotor in a climb; magnitude(top), phase(bottom)

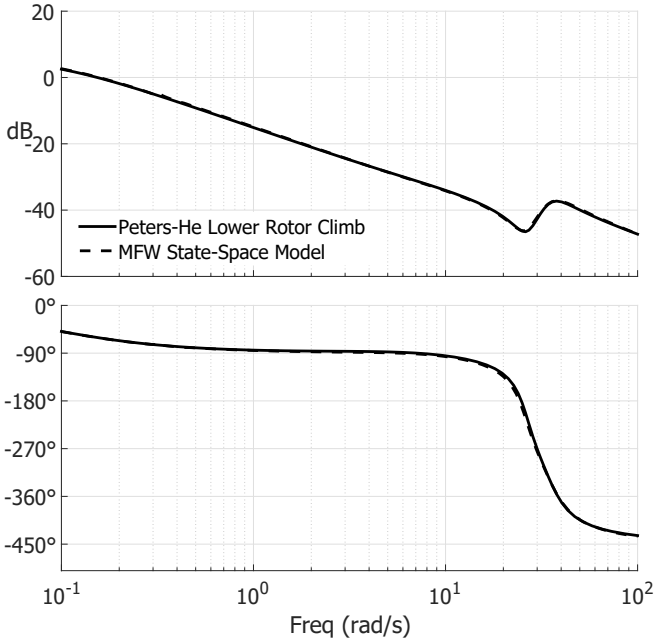

Fig. 11. Responses of yaw rate r to θ_0^D showing comparison between MFW identified state-space model and Peters-He model with the lower rotor in a climb; magnitude(top), phase(bottom)

Figure 16 shows a bode plot of the $\bar{v}_z$ due to many thrust perturbation (ΔC_T) at different frequencies across the frequency range. The plot shows that the points across the tail exhibit similar behavior and can be all approximately represented by

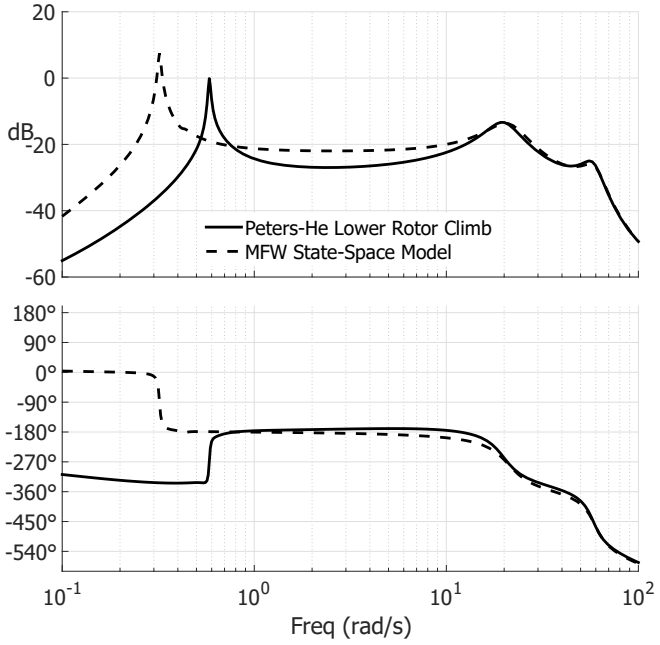

Fig. 12. Responses of roll rate p to θ_{1S}^{S} showing comparison between MFW identified state-space model and Peters-He model with the lower totor in a climb; magnitude(top), phase(bottom)

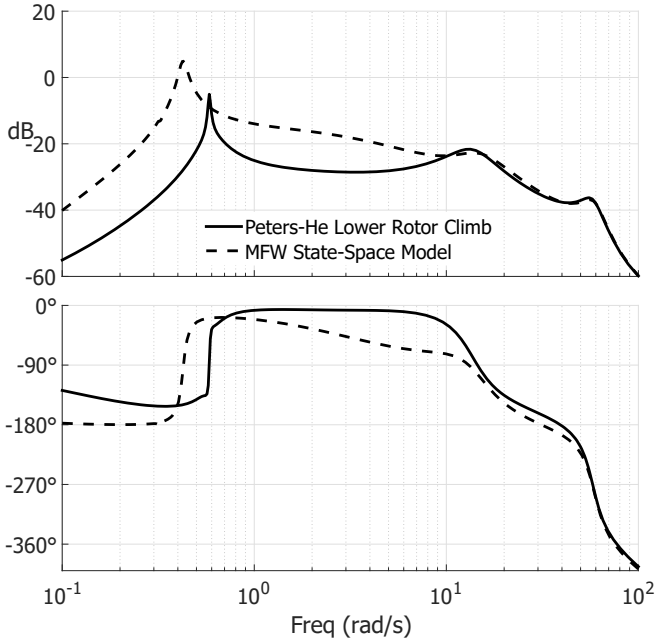

Fig. 13. Responses of pitch rate q to θ_{1C}^{S} showing comparison between MFW identified state-space model and Peters-He model with the lower rotor in a climb; magnitude(top), phase(bottom)

the tail average. This result is also compared with the induced velocity inside the wake (at $r/R = 0.75$), which as expected is evidently much higher with a sign difference. This bode plot can further be approximately expressed as an ODE, by

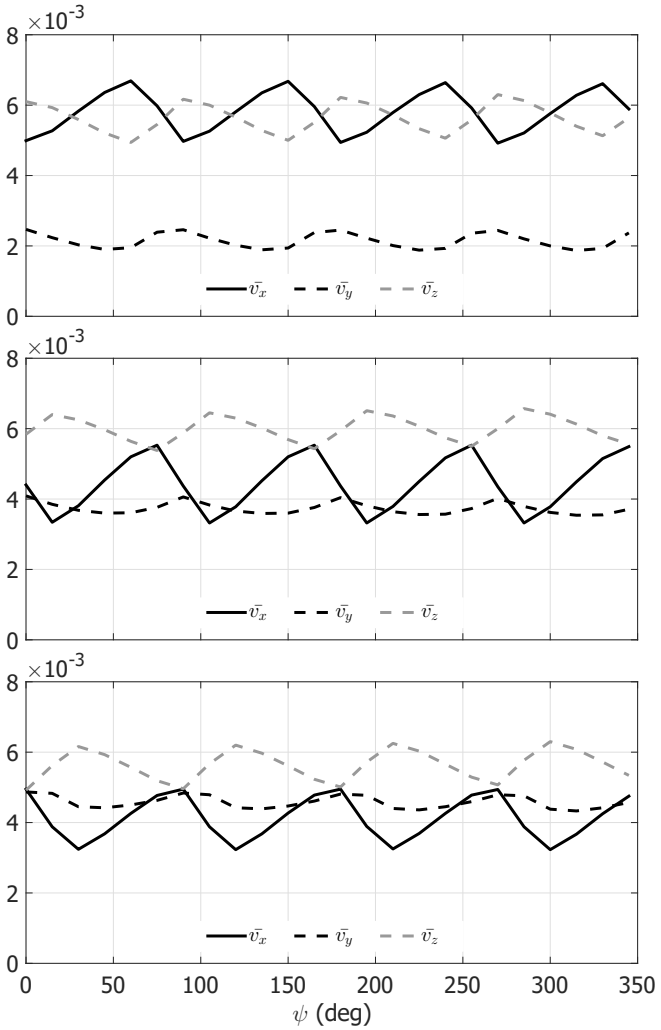

Fig. 14. RFW rotor induced velocity at the horizontal tail vs. azimuth angle of blade #1 (no excitation); port tip(top), center point(middle), starboard tip(bottom)

the method shown in Refs. 7, 25.

Figure 17 shows $\bar{v}_z$ due to pitch perturbation (ΔC_M) in hover (trim C_T=0.005). Again, it is shown that the behavior is similar for the various points on the tail and much lower than those which are located inside the wake.

Tail Output-Equation Induced Inflow Results – MFW The methodology described to identify output-equation off-rotor induced inflow was performed on the MFW to come up with the relationship between $\boldsymbol{\lambda}$ and $\bar{v}_x$, $\bar{v}_y$ and $\bar{v}_z$ for a single main rotor in hover. For the location of the tail, the average of the seven points across the 1/4 chord line was used. Using the form defined by Eq 11, the output equation for the induced

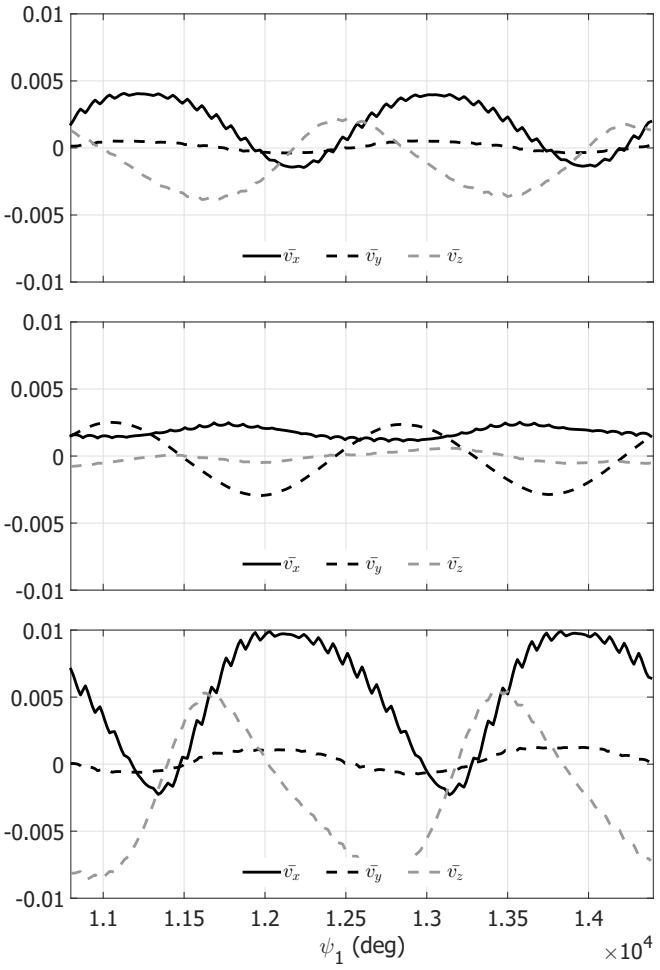

Fig. 15. RFW induced velocities at the tail center point due to ΔC_T (top), ΔC_L (middle), and ΔC_M (bottom) perturbations in hover

velocities was determined to be:

$$\begin{Bmatrix} \bar{v}_x \\ \bar{v}_y \\ \bar{v}_z \end{Bmatrix} = \begin{bmatrix} -0.2892 & -0.3108 & 0.0532 \\ -0.142 & -0.1353 & 0.3407 \\ 0.3148 & 0.5361 & -0.1104 \end{bmatrix} \times \begin{Bmatrix} \lambda_0(t-0.06225) \\ \lambda_{1c}(t-0.2115) \\ \lambda_{1s}(t-0.6929) \end{Bmatrix} \quad (19)$$

Figure 18 shows the time-domain verification of the output equations for tail inflow. This was performed using a ramp input, and time histories calculated from the state-space model are compared to the actual output of the MFW. The time-domain verification shows that the system responds well in the long term, but has some misalignment in the short term at high frequency. The error here is attributable to the fact that the velocities have been approximated to be a linear combination of the inflow coefficients, and the responses were only fit at low frequency. Hence the verification is not expected to be exact, but rather adequate enough to provide the needed dynamics.

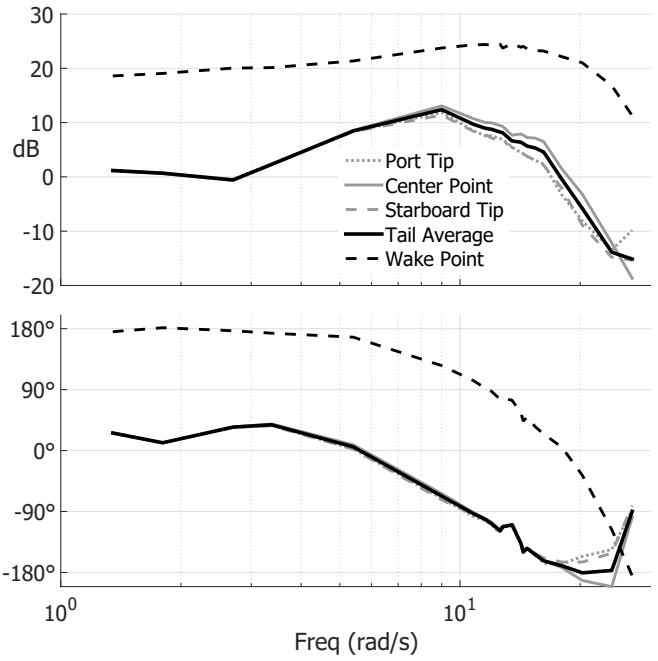

Fig. 16. Responses of $\bar{v}_z$ due to ΔC_T in hover (trim C_T=0.005) at various points across the tail and at a point inside the wake using RFW; magnitude(top), phase(bottom)

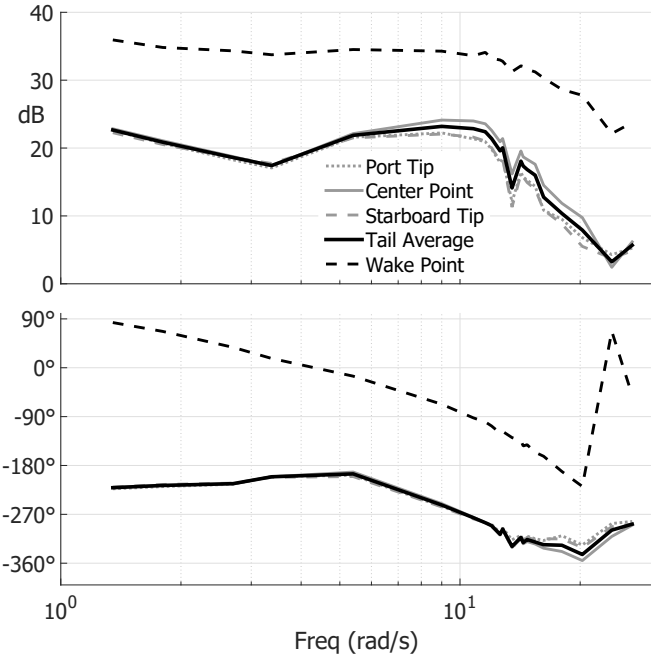

Fig. 17. Responses of $\bar{v}_z$ due to ΔC_M in hover (trim C_T=0.005) at various points across the tail and at a point inside the wake using RFW; magnitude(top), phase(bottom)

Fuselage Output-Equation Induced Inflow Results – MFW Another example example of Output-Equation Induced Inflow can be shown for points which are directly in the wake. Once again this was performed on a single main

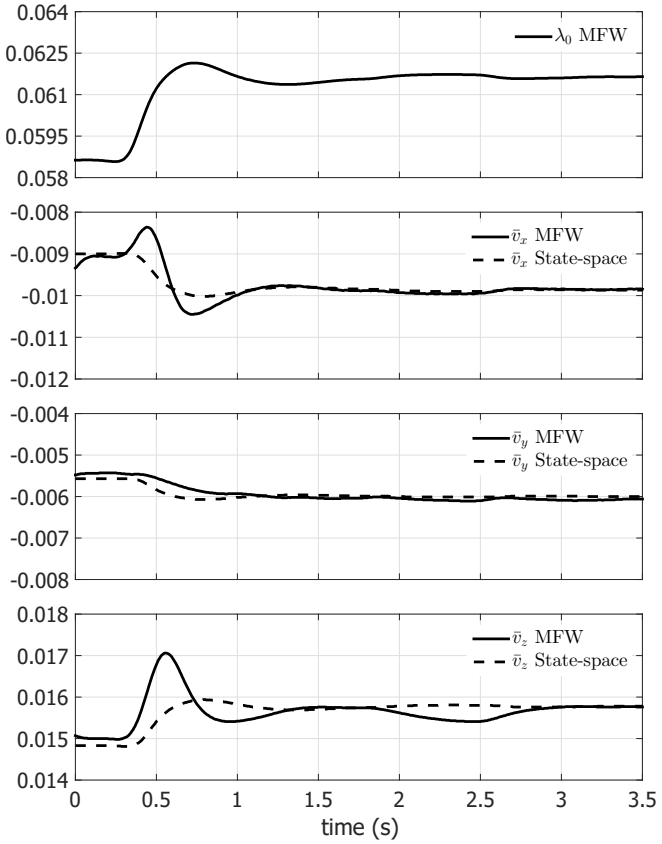

Fig. 18. Time-domain verification of off-rotor tail inflow given a ramp in λ_0 (compared with MFW)

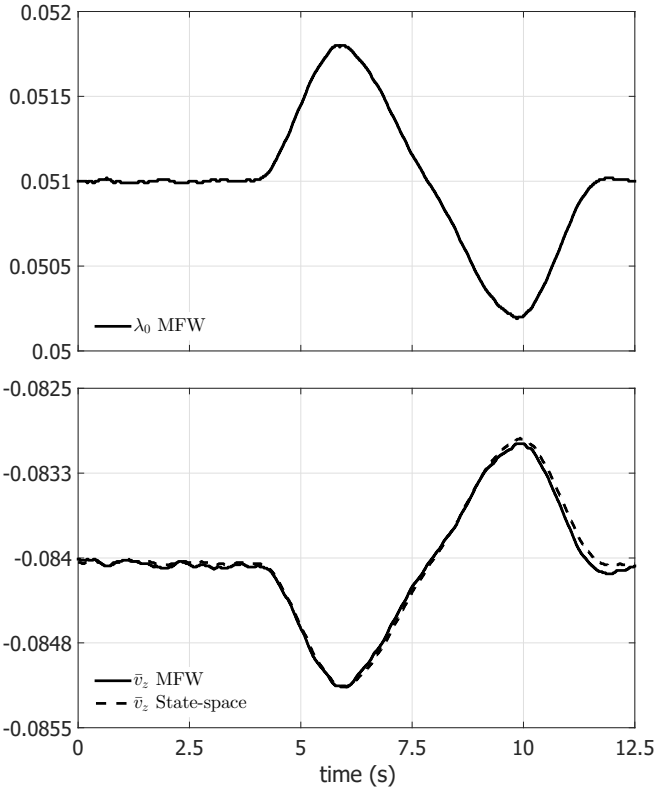

Fig. 19. Time-domain verification of off-rotor fuselage inflow given a doublet in λ_0 (compared with MFW)

rotor in hover using the MFW. The output equation, fit to the form defined by Eq 12, is defined as:

$$\begin{Bmatrix} \bar{v}_x \\ \bar{v}_y \\ \bar{v}_z \end{Bmatrix} = \begin{bmatrix} 0.0221 & -0.7496 & -0.2117 \\ 0 & 0.207 & -0.766 \\ -1.366 & 0.02861 & 0 \end{bmatrix} \circ \left(\left(t - \begin{bmatrix} 0.2149 & 0.541 & 0.3795 \\ 0 & 0.4452 & 0.5327 \\ 0.07075 & 0.154 & 0 \end{bmatrix} \right) \times \begin{Bmatrix} \lambda_0 \\ \lambda_{1c} \\ \lambda_{1s} \end{Bmatrix} \right) \tag{20}$$

The time-domain verification of these output equations are shown by Figure 19. This time a doublet input is used, and the time histories calculated by the state-space model are compared to the actual output of the MFW. For this case, a perturbation in λ_0 only produces a significant perturbation in $\bar{v}_z$. For this case the output equations are a much better fit, indicating that the velocities in the wake are well represented by this formulation. This is important since a point inside the wake experiences the larger induced velocities which can actually create disturbances in the aircraft dynamics.

CONCLUSIONS

This paper presents a frequency domain system identification methodology to extract a low order rotor inflow model in the form of a system of ODEs, suitable for flight dynamics and control applications. The methodology is demonstrated using a free-vortex wake simulation, but it is applicable to a wide variety of advanced aerodynamic analyses, including CFD-based ones. The methodology can also be applied to extract state-space models of the inflow at points away from the rotor disk, such as fuselage and empennage.

The wake dynamics describing the relationship from rotor loads to inflow were extracted as non-parametric frequency responses. These responses showed that this type of dynamics of the rotor wake is linear in the frequency range of interest in flight dynamics. Each non-parametric response had generally high coherence across that frequency range.

The non-parametric frequency responses were fit with a first order state-space model, which allows coupling and interference between the rotors. In general, the state space model fit well the collective responses, but mis-alignment was found in the lateral and longitudinal inflow responses when compared to the free-wake frequency responses. It is possible that a higher order model could be created to better capture the shape of the non-parametric frequency responses. Even simple second order models for each of the given frequency responses would likely improve the accuracy of the identification. Higher order models come at the cost of model complexity and loss of insight into the physical meaning of the inflow states. In the first order model presented, the states are the inflow coefficients, but further analysis would need to be done to determine the physical meaning of any higher order states. For this reason, the first order model is used in this paper.

The identified state-space model was then used in a full aircraft simulation model. Comparisons of the predicted aircraft response to controls using the identified state space model and a simple modification of the single rotor Peters-He model were given. The results show that for the heave and yaw responses, the inflow models predicted very similar behavior. The responses to pitch and roll inputs show quite different responses, indicating that a more complex model with rotor-rotor interactions is needed to properly predict the aircraft behavior.

Lastly two methods were presented to approximately predict the inflow of any point off of the rotor. The first was a full ODE model describing the relationship between rotor loads and off-rotor inflow. This has the advantage of offering an accurate prediction across the frequency range of flight perturbations. The second method was to compute off-rotor inflow as a linear combination of the on-rotor inflow states. This has the advantage of not needing extra states, however this advantage may be negated by the need for additional states arising from the Padé approximations to the time delays.

The time-domain verification results show that the approximation is reasonably accurate. It is also important to note that, with little effort, the frequency sweep method could be used to achieve the full ODE model of off-rotor inflow, and likewise the single frequency analysis could determine an output-equation inflow model.

In conclusion, the results of this paper show that:

1. Given a high-fidelity non-linear aerodynamic simulation of coaxial rotor inflow, it is possible to extract a linear model that well represents the inflow dynamics at a given trim condition.

2. A first-order linear inflow model does not capture all of the dynamics of a coaxial rotor wake, and a higher order model may be required to get a better match with the free wake data.

3. An ODE model or an output equation on the inflow ODE model can be extracted and used to predict the rotor-induced velocities anywhere on or around the aircraft.

4. When coupled back into a full flight simulation, some differences between the identified model and a more classical dynamic inflow-type model exist, showing the necessity of a coupled rotor inflow model.

Because of the complexity of a coaxial rotor flow field and, in general, of the flow fields away from the rotor and especially in proximity of fuselage and empennage, the conclusions above should be carefully validated with more refined mathematical models and experiment.

Author contact: Sean Hersey shersey@terpmail.umd.edu, Roberto Celi celi@umd.edu

ACKNOWLEDGMENTS

This research work was conducted under the US-Israel Rotorcraft Project Agreement. The computer code for the Maryland Free Wake was developed and made available by Dr. J. G. Leishman.

REFERENCES

[1]Peters, D. A. and He, C. J., "Correlation of Measured Induced Velocities with a Finite-State Wake Model," *Journal of the American Helicopter Society*, Vol. 36, (3), July 1991, pp. 59–70.

[2]Prasad, J. V. R., Nowak, M., and Xin, H., "Finite State Inflow Models for a Coaxial Rotor in Hover," 38th European Rotorcraft Forum Proceedings, Amsterdam, Netherlands, September 2012.

[3]Nowak, M., Prasad, J. V. R., Xin, H., and Peters, D. A., "A Potential Flow Model for Coaxial Rotors in Forward Flight," 39th European Rotorcraft Forum Proceedings, Moscow, Russia, September 2013.

[4]Nowak, M., Prasad, J. V. R., and Peters, D. A., "Development of a Finite State Model for a Coaxial Rotor in Forward Flight," American Helicopter Society 70th Annual Forum Proceedings, Montréal, Canada, May 2014.

[5]Xin, H., Goss, J. D., and Parkes, C., "Development of a Three-State Rotor Interference Model and Application to Coaxial Rotor Inflow Modeling," American Helicopter Society Aeromechanics Specialists Conference Proceedings, San Francisco, CA, January 2014.

[6]Yong-Boon, K., Prasad, J., Sankar, L., and Kim, J., "Finite State Coaxial Rotor Inflow Model Improvements via System Identification," American Helicopter Society 72th Annual Forum Proceedings, West Palm Beach, FL, May 2016.

[7]Rand, O., Khromov, V., Hersey, S., Celi, R., Juhasz, O., and Tischler, M. B., "Linear Inflow Model Extraction From High-Fidelity Aerodynamic Models for Flight Dynamics Applications," American Helicopter Society 71st Annual Forum Proceedings, Virginia Beach, VA, May 2015.

[8]Pitt, D. M. and Peters, D. A., "Theoretical Prediction of Dynamic Inflow Derivatives," *Vertica*, Vol. 5, (1), 1981, pp. 21–34.

[9]Peters, D. A. and HaQuang, N., "Dynamic Inflow for Practical Applications," *Journal of the American Helicopter Society*, Vol. 33, (4), October 1988, pp. 64–68.

[10]Gennaretti, G. R. S. J. B. G., M. and Cardito, F., "Rotor Dynamic Wake Inflow Finite-State Modelling," 33rd AIAA Applied Aerodynamics Conference, Dallas, TX, June 2015. doi: 10.1007/s13272-016-0235-y

[11]Gennaretti, G. R. S. J. e. a., M., "Identification of rotor wake inflow finite-state models for flight dynamics simulations," *CEAS Aeronautical Journal*, Vol. 8, (1), March 2017, pp. 209–230.
doi: 10.1007/s13272-016-0235-y

[12]Johnson, W., Moodie, A. M., and Yeo, H., "Design and Performance of Lift-Offset Rotorcraft for Short-Haul Missions," American Helicopter Society Future Vertical Lift Aircraft Design Conference Proceedings, San Francisco, CA, January 2012.

[13]Ruddell, A. J., "Advancing Blade Concept (ABC) Technology Demonstrator," USAAVRADCOM TR-81-D-5, April 1981.

[14]Fegely, C., Xin, H., Juhasz, O., and Tischler, M. B., "Flight Dynamics and Control Modeling with System Identification Validation of the Sikorsky X2 Technology Demonstrator," American Helicopter Society 72nd Annual Forum Proceedings, West Palm Beach, FL, May 2016.

[15]Harendra, P. B., Joglekar, M. J., Gaffey, T. M., and Marr, R. L., "Final Report V/STOL Tilt Rotor Study - Volume V: A Mathematical Model for Real Time Flight Simulation of the Bell Model 301 Tilt Rotor Research Aircraft," NASA CR 114614, April 1973.

[16]Bailey Jr., F. J., "A Simplified Theoretical Method of Determining the Characteristics of a Lifting Rotor in Forward Flight," NACA-TR 716, January 1941.

[17]Bhagwat, M. J. and Leishman, J. G., "Time-Accurate Modeling of Rotor Wakes Using A Free-Vortex Wake Method," *Journal of Aircraft*, Vol. 39, (5), September-October 2002, pp. 759–775.

[18]Rand, O. and Khromov, V., "Compound Helicopter: Insight and Optimization," *Journal of the American Helicopter Society*, Vol. 60, (1), January 2015, pp. 012001–1012001–12.

[19]Rand, O., "RAPiD - Rotorcraft Analysis for Preliminary Design, User Guide – 2012," TAE 987 Report, Technion - Israel Institute of Technology, Faculty of Aerospace Engineering, 2012.

[20]Leishman, J. G., Bhagwat, M. J., and Bagai, A., "Free-Vortex Filament Methods for the Analysis of Helicopter Rotor Wakes," *Journal of Aircraft*, Vol. 39, (5), September-October 2002.

[21]Bhagwat, M. J. and Leishman, J. G., "Accuracy of Straight-Line Segmentation Applied to Curvilinear Vortex Filaments," *Journal of the American Helicopter Society*, Vol. 46, (2), April 2001, pp. 166–169.

[22]Weissinger, J., "The Lift Distribution of Swept-Back Wings," NACA TM 1120, 1947.

[23]Leishman, J., *Principles of Helicopter Aerodynamics*, Cambridge University Press, New York, NY, second edition, Chapter 8, 2006.

[24]Tischler, M. B. and Remple, R. K., *Aircraft and Rotorcraft System Identification: Engineering Methods with Flight Test Examples*, AIAA, Reston, VA, 2006.

[25]Rand, O. and Khromov, V., "Free-Wake Based Dynamic Inflow Model for Hover, Forward and Maneuvering Flight," American Helicopter Society 72nd Annual Forum Proceedings, West Palm Beach, FL, May 2016.

[26]Celi, R., "HeliUM 2 Flight Dynamic Simulation Model: Developments, Technical Concepts, and Applications," American Helicopter Society 71st Annual Forum, Virginia Beach, VA, May 2015.

[27]Celi, R., "Helicopter Rotor Blade Aeroelasticity in Forward Flight with an Implicit Structural Operator," *AIAA Journal*, Vol. 30, (9), 1992.

[28]Johnson, W., *Helicopter Theory*, Princeton University Press, Princeton, NJ, 1980, pp. 469–544.

[29]Franklin, G., Powell, D., and Emani-Naeini, A., *Feedback Control of Dynamic Systems*, Prentice Hall, Upper Sadle River, NJ, fourth edition, 2002, pp. 331–334.

APPENDIX

Table 3. Aircraft poles with Peters-He inflow with climbing lower rotor.

Freq. (rad/s)	Pole		Description
0	0		heading
0.08656	-0.08656		heave
0.478	-0.478		yaw
0.5833	0.007835	± 0.5833i	phugoid
0.5858	0.0852	± 0.5796i	phugoid
2.788	-2.788		spiral
4.18	-4.18		pitch
10.29	-10.29		inflow
11.44	-11.44		inflow
13.68	-3.705	± 13.17i	Regressive Flap
19.28	-19.28		inflow
19.79	-19.79		inflow
19.87	-3.747	± 19.51i	Regressive Flap
21.4	-21.4		inflow
21.71	-21.71		inflow
34.71	-7.631	± 33.86i	Coning Flap
35.36	-7.975	± 34.45i	Reactionless Flap
35.43	-7.34	± 34.66i	Reactionless Flap
35.53	-6.849	± 34.86i	Coning Flap
57.92	-7.262	± 57.46i	Progressive Flap
58.34	-6.572	± 57.97i	Progressive Flap

Table 4. Aircraft poles with MFW identified state-space model inflow.

Freq. (rad/s)	Pole		Description
0	0		heading
0.08606	-0.08606		heave
0.321	-0.005125	± 0.3209i	phugoid
0.4252	0.02015	± 0.4247i	phugoid
0.8566	-0.8566		yaw
3.23	-3.23		pitch
3.799	-3.798	± 0.0969i	inflow
3.853	-3.853		inflow
3.853	-3.853		inflow
4.455	-4.455		pitch
4.93	-4.93		pitch
7.408	-7.408		inflow
9.985	-9.179	± 3.931i	inflow
10.89	-10.89		inflow
12.44	-10.93	± 5.95i	inflow
13.62	-12.93	± 4.284i	inflow
13.79	-13.79		inflow
13.79	-13.79		inflow
14.43	-11.58	± 8.604i	inflow
14.94	-4.736	± 14.17i	Regressive Flap
21.05	-4.601	± 20.54i	Regressive Flap
21.85	-21.85		inflow
25.54	-22.07	± 12.86i	inflow
28.47	-23.85	± 15.54i	inflow
34.83	-8.367	± 33.81i	Coning Flap
35.08	-30.72	± 16.93i	inflow
35.36	-7.804	± 34.49i	Reactionless Flap
35.39	-7.576	± 34.57i	Reactionless Flap
35.92	-7.663	± 35.1i	Coning Flap
41.47	-35.94	± 20.68i	inflow
42.91	-37.06	± 21.63i	inflow
49.94	-49.94		inflow
58.92	-7.512	± 58.43i	Progressive Flap
59.3	-7.376	± 58.84i	Progressive Flap
68.53	-68.53		inflow
88.76	-88.73	± 2.535i	inflow